TPEL-Reg-2017-07-1328.R2

Partially-Isolated Single-Magnetic Multi-Port Converter Based on Integration of Series-Resonant Converter and Bidirectional PWM Converter

Masatoshi Uno, *Member, IEEE*, Rina Oyama, and Kazuki Sugiyama

***Abstract*— Recent power systems, such as renewable energy systems consisting of solar panels and rechargeable batteries, contain multiple power sources and need multiple converters in proportion to the number of power sources, resulting in increased system complexity and cost. This paper proposes a multi-port converter (MPC) integrating a bidirectional PWM converter and series-resonant converter. Not only is the switch count halved with the proposed MPC but also magnetic components can be integrated, reducing the circuit complexity and volume. A 150-W prototype of the proposed MPC was built for the experimental verification. The measured voltage conversion characteristics and transient responses demonstrated that the proposed MPC could control load and battery voltages independently by PWM and PFM controls, respectively.**

***Index Terms* — Integration, PWM converter, series-resonant converter, multi-port converter**

NOMENCLATURE

CC	Constant-current
CT	Center-tapped
CV	Constant-voltage
DAB	Dual active bridge
FHA	Fundamental harmonics approximation
MPC	Multi-port converter
MPPT	Maximum power point tracking
PFM	Pulse frequency modulation
PS	Phase shift
PWM	Pulse width modulation
SR	Synchronous rectifier
SRC	Series-resonant converter

Manuscript received July 16, 2017, revised October 6 and December 6, 2017; accepted January 9, 2018. This work was supported by the Mazda Foundation Grant 2016.

M. Uno and K. Sugiyama are with the Faculty of Engineering, Ibaraki University, Hitachi 316-8511, Japan (e-mail: masatoshi.uno.ee@vc.ibaraki.ac.jp; 16nm621x@vc.ibaraki.ac.jp).

Rina Oyama is with Hitachi City Hall, Hitachi, Japan (email: sky.rina.32756927@gmail.com).

I. INTRODUCTION

Recently, power systems are increasingly becoming complex as they contain multiple power sources and loads. Photovoltaic systems, for example, contain not only solar panels but also rechargeable batteries to buffer fluctuations in power generation of solar panels. Electric vehicles also consist of multiple power sources including not only a generator but also high-, medium- (48 V), and low-voltage (12 V) batteries for various kinds of loads. In such power systems, multiple converters are necessary to individually control each power source, increasing the system complexity and cost, as shown in Fig. 1(a).

To reduce the number of converters necessary in such power systems, multi-port converters (MPCs) that combine multiple converters into a single unit have been proposed [see Fig. 1(b)]. MPCs are categorized into roughly three groups: isolated, partially-isolated, and non-isolated MPCs. The most representative isolated MPC topology is the triple active bridge converter [1]–[5] that is the extended version of traditional dual active bridge (DAB) converters. Input/output ports can be extended by adding windings and inverter bridges. However, each input/output port requires four switches (or two switches for half-bridge topologies), and hence, this topology tends to suffer from the complex circuit due to the large switch count. Meanwhile, non-isolated MPCs are undoubtedly suitable for non-isolated applications thanks to the reduced switch count as well as the lack of bulky and lossy transformers [6]–[14].

Various kinds of partially-isolated MPCs have been proposed [15]–[31]. These MPCs can be derived from the combination of a bidirectional PWM converter and isolated full- or half-bridge converters [17]–[20] or phase-shift converters [22]–[29]. A

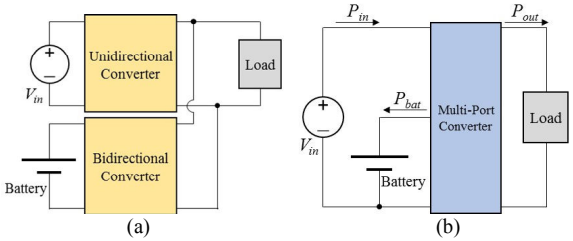

Fig. 1. (a) Traditional power system with multiple converters, (b) multi-port converter system.

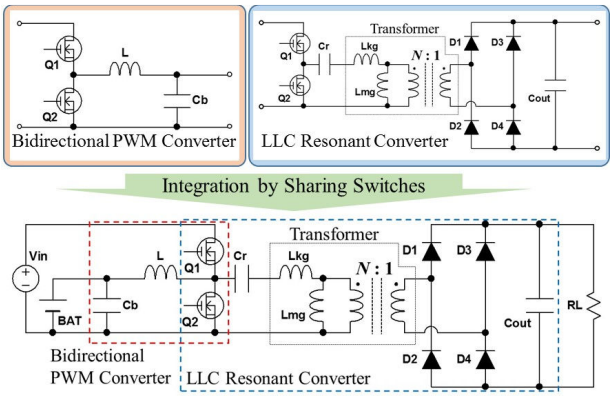

Fig. 2. Derivation of conventional partially-isolated MPC from the integration of bidirectional PWM converter and LLC resonant converter.

brief example procedure to integrate the PWM and half-bridge LLC resonant converters is illustrated in Fig. 2. Two converters are integrated by sharing switches (Q_1 and Q_2), hence halving the total switch count. The benefit of the integration, however, is not significant as only two switches are eliminated from traditional power systems using two separate converters shown in Fig. 1(a). Especially, magnetic components used in each separate converter (an inductor for the PWM converter and a transformer for the LLC converter) firmly remain in the derived MPC, suggesting the challenge of circuit miniaturization.

This paper proposes the single-magnetic partially-isolated MPC integrating a series-resonant converter (SRC) and bidirectional PWM converter. In the proposed MPC, the magnetizing inductance of the transformer is utilized as a filter inductor for the PWM converter, while the leakage inductance plays a role of a resonant inductor for the SRC, thus achieving the single-magnetic topology. Section II deals with the derivation procedure and major features of the proposed MPC. Section III discusses the power flow and operation mode of the MPC. The detailed operation analyses in battery charging and discharging modes will be performed in Sections IV and V, respectively. The design guideline will be presented in Section VI, followed by the experimental verification in Section VII.

II. Single-Magnetic Partially-Isolated MPC

A. Derivation

The proposed partially-isolated MPC is derived from the combination of the bidirectional PWM converter and SRC, as shown in Fig. 3. Similar to the MPC shown in Fig. 2, switches are shared by two converters. For the unidirectional input port, such as photovoltaic panels, a reverse blocking diode D_{block} is placed at the input port.

The prominent feature of the derived MPC is that the transformer is also shared, realizing the single-magnetic topology. The leakage inductance L_{kg} is utilized as the resonant inductor, while the magnetizing inductance L_{mg} behaves as a filter inductor for the PWM converter. In other words, the transformer plays two roles. The minor difference from the MPC shown in Fig. 2 is that C_r is placed on the secondary side

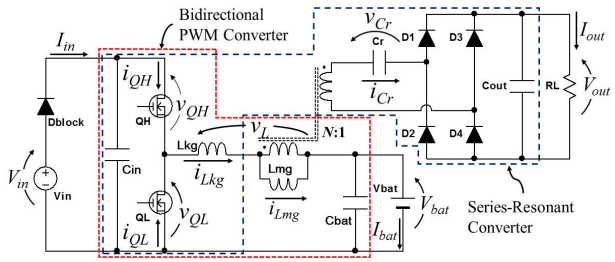

Fig. 3. Proposed partially-isolated single-magnetic MPC integrating bidirectional PWM converter and series-resonant converter.

because of the dc current component of the primary winding—the primary winding corresponds to a filter inductor in traditional PWM converters that contains a dc current component. The resonant capacitor C_r resonates with L_{kg} only, and therefore, the resonant operation of the proposed MPC is identical to that of conventional SRCs, not LLC converters—C_r resonates with both L_{kg} and L_{mg} in LLC converters. For more detailed discussion for the comparison between LLC converters and the SRC in the proposed MPC, refer to Appendix Section.

B. Features

Similar to the conventional MPCs, two separate converters can be integrated into a single unit, simplifying the system by reducing the component count. In addition, the circuit-level simplification is also feasible due to the reduced switch count—the switch count is an index to represent the circuit complexity as each switch requires several ancillary elements including a gate driver IC and its auxiliary power supply.

The single-magnetic topology is the remarkable benefit of the proposed MPC. Conventional partially-isolated and non-isolated MPCs require more than two magnetic components because they are essentially the combination of two different converters, and each of them requires an inductor or transformer. The MPC shown in Fig. 2, for example, requires an inductor and transformer for the PWM-controlled bidirectional converter and PFM-controlled LLC converter, respectively. The proposed MPC, on the other hand, requires only one transformer that is the key component and plays two roles as a filter inductor and resonant inductor, as will be detailed in Section III. The single-magnetic topology potentially contributes to reducing the circuit volume and footprint.

Most conventional partially-isolated MPCs employ two modulation schemes (e.g., PWM and PFM controls, or PWM and phase-shift controls) in order to regulate two power sources individually. However, since two converters are integrated into a single unit, the interdependence between two control schemes is observed [14], [17], depending on operation conditions. In other words, decoupled output regulation is not feasible. Although the interdependence issue can be precluded by introducing the decoupling network [14], [17], the mathematical derivation based on the state-space model for the decoupling network might be a design hurdle, especially for resonant converters, for which the state-space model analysis is a daunting challenge.

Similar to the conventional partially-isolated MPCs, the

proposed MPC utilizes two control freedoms of duty cycle d and switching frequency f_S for PWM and PFM controls, respectively. But the proposed MPC offers the benefit of the decoupled output regulation. By operating the MPC so that the sinusoidal resonant current is discontinuous, the interdependence can be avoided, achieving the decoupled output regulation, as will be detailed in Section IV.

The drawbacks include the narrow voltage regulation range of the SRC and increased peak current of the high-side switch Q_H due to the current superposition, as will be discussed in Sections IV-D and III-C, respectively. Another drawback is that one single failure of circuit elements in the MPC might lead to the failure of the entire system, similar to conventional MPCs—for example, both V_{out} and V_{bat} are no longer regulated if one of the switches fails.

III. Power Flow and Operation Modes

In this paper, the proposed MPC is assumed to have one unidirectional input port (V_{in}), one bidirectional port (V_{bat}), and one unidirectional output port (V_{out}). Unidirectional power sources, such as fuel cells, solar panels, and generators, are connected to the unidirectional input port, while rechargeable batteries are for the bidirectional port. The power balance in the MPCs is given by the simple equation as

$$P_{in} = P_{out} + P_{bat}, \tag{1}$$

where P_{in}, P_{out}, and P_{bat} are the input, output, and battery charging powers, respectively, as designated in Fig. 1(b). This simple equation suggests that controlling two of three powers automatically determines the rest one. As briefly mentioned in Section II, the proposed MPC has two control freedoms of duty cycle d and switching frequency f_S for PWM and PFM controls, respectively. The PWM and PFM controls are used to control two of three powers in (1).

Depending on the power balance, the MPC operates in either the battery charging mode, hybrid mode, or battery discharging mode, as shown in Fig. 4.

Battery Charging Mode ($P_{in} > P_{out}$): The input power source V_{in} is capable of supplying P_{out}. P_{out} (or V_{out}) and P_{bat} (or V_{bat}) are regulated by the PFM-controlled SRC and PWM converter, respectively. The detailed operation analysis for the battery charging mode will be performed in Section IV.

Hybrid Mode ($P_{in} < P_{out}$): P_{out} exceeds P_{in}, and P_{bat} becomes negative, meaning the battery starts discharging to support the input power source. P_{in} or the input current is controlled by the PWM converter—for examples, maximum power point tracking (MPPT) for solar panels and constant-current control for fuel cells. Meanwhile, P_{out} (or V_{out}) is regulated by the SRC with PFM control. This mode is very similar to the battery charging mode in terms of switching mode (see Fig. 6) and mathematical equations (see Sections IV). Therefore, detailed explanation for this mode is not presented to save page length.

Battery Discharging Mode ($P_{in} = 0$): The input power source is not available (e.g., solar panels at night), and hence, the battery alone has to supply all the load power. The MPC in this mode is equivalent to a single-input–single-output converter,

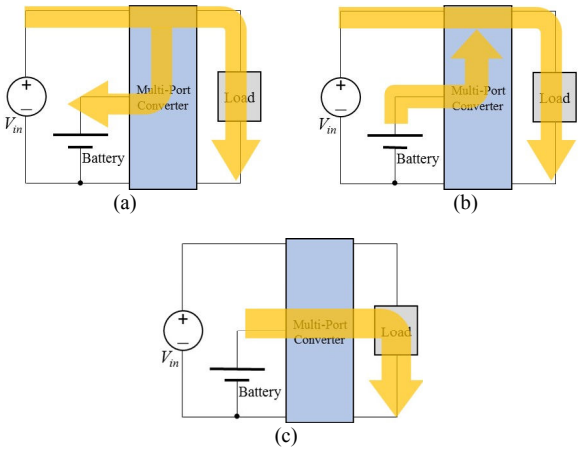

Fig. 4. Power flow in (a) battery charging mode, (b) hybrid mode, and (c) battery discharging mode.

although there are two control freedoms of d and f_S. The optimized switching frequency PWM control is employed to regulate P_{out}, as will be discussed in detail in Section V.

IV. Operation Analysis for Battery Charging Mode

A. Operation Principle

The operation analysis is performed based on the premise that all the circuit elements are ideal, L_{mg} is far larger than L_{kg} ($L_{mg} >> L_{kg}$), and a dead time is negligibly short. The theoretical (simulation) key operation waveforms and current flow directions in the battery charging mode are shown in Figs. 5(a) and 6, respectively. The high- and low-side switches, Q_H and Q_L, are driven in complementary mode, and therefore, the bidirectional PWM converter operates in continuous conduction mode (CCM).

Mode 1 [Fig. 6(a)]: Q_H is turned on, and the current of L_{mg}, i_{Lmg}, starts linearly increasing. The voltage of the transformer primary winding v_L is equal to $V_{in} - V_{bat}$, by which the SRC is driven. The resonant capacitor C_r on the secondary winding and the leakage inductance L_{kg} starts resonating, and sinusoidal resonant current i_{Cr} flows through D_1 and D_4 in the diode bridge. Hence, the current of Q_H, i_{QH}, and i_{Lkg} are equivalent to i_{Lmg} with i_{Cr}/N superimposed on it (N is the transformer turns ratio). The length of Mode 1 is equal to half the resonant period, and the operation moves to the next mode as i_{Cr} becomes zero.

i_{Lmg} in Mode 1 (as well as Mode 2) is expressed as

$$i_{Lmg}(t) = I_{bat} - \frac{\Delta I_{Lmg}}{2} + \frac{V_{in} - V_{bat}}{L_{mg}} t, \tag{2}$$

where I_{bat} is the average current of i_{Lmg}, and ΔI_{Lmg} is the ripple current of i_{Lmg}, which is given by

$$\Delta I_{bat} = \frac{V_{in} - V_{bat}}{L_{mg}} dT_S = \frac{V_{bat}}{L_{mg}}(1-d)T_S, \tag{3}$$

where d is the duty cycle of Q_H, and T_S is the switching period. i_{Lkg} is equal to the sum of i_{Lmg} and reflected current of i_{Cr}, as

$$i_{Lkg}(t) = i_{Lmg}(t) + \frac{1}{N} I_m \sin \omega_r t, \tag{4}$$

where I_m is the amplitude of i_{Cr} as designated in the Fig. 5(a),

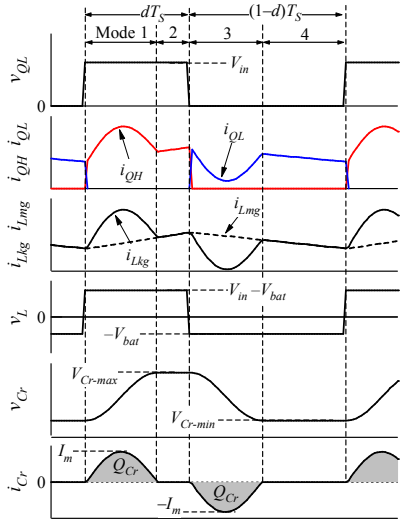

(a)

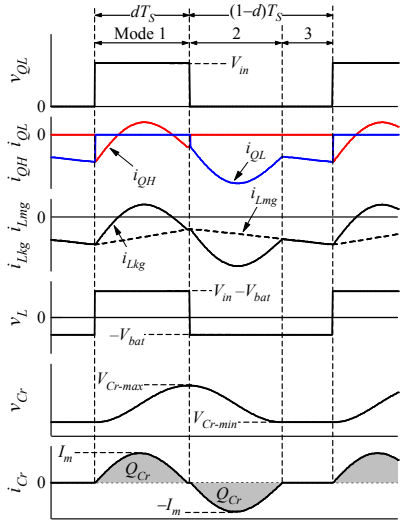

(b)

Fig. 5. Key operation waveforms in (a) battery charging mode and (b) battery discharging mode.

and ω_r (= $2\pi f_r$) is the resonant angular frequency given by

$$\omega_r = 2\pi f_r = \frac{1}{\sqrt{L_{kg} C_r / N^2}}. \tag{5}$$

Mode 2 [Fig. 6(b)]: i_{Lmg} still linearly increases, while no current flows in the diode bridge on the secondary side, and hence, the SRC is essentially inactive. Therefore, this operation mode is identical to the on-period of ordinary PWM converters.

Mode 3 [Fig. 6(c)]: Q_H is turned-off, and i_{Lkg} is commutated to Q_L. The polarity of v_L is reversed as $-V_{bat}$, and i_{Cr} starts flowing through D_2 and D_3. Hence, the current of Q_L, i_{QL}, is equal to i_{Lmg} with i_{Cr}/N superimposed on it. The length of this mode is equal to half the resonant period, similar to Mode 1. As i_{Cr} reaches zero again, the operation moves to the next mode.

i_{Lmg} in Mode 3 (as well as Mode 4) is

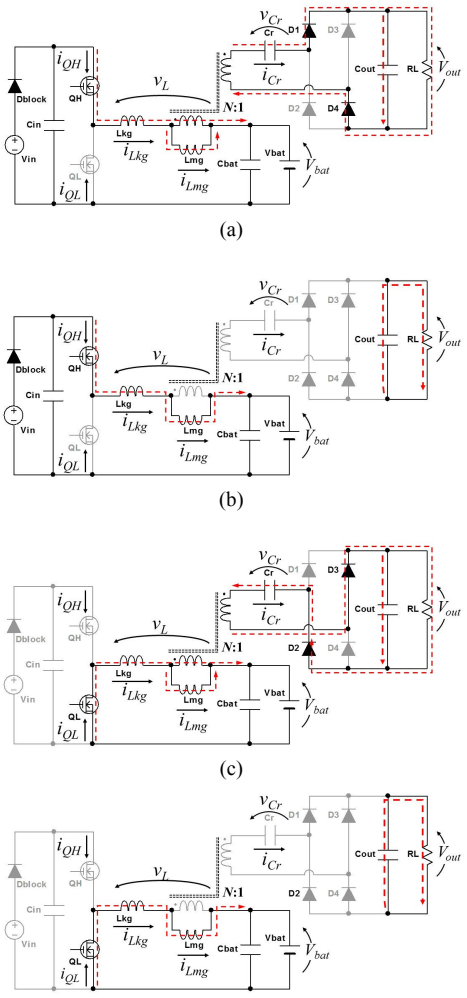

(a) (b) (c) (d)

Fig. 6. Operation modes in battery charging mode: (a) Mode 1, (b) Mode 2, (c) Mode 3, (d) Mode 4.

$$i_{Lmg}(t) = I_{bat} + \frac{\Delta I_{bat}}{2} - \frac{V_{bat}}{L_{mg}}(t - dT_S). \tag{6}$$

Similar to Mode 1, i_{Cr}/N is superimposed on i_{Lmg}, and therefore, i_{Lkg} is yielded as

$$i_{Lkg}(t) = i_{Lmg}(t) - \frac{1}{N} I_m \sin(\omega_r t - dT_S). \tag{7}$$

Mode 4 [Fig. 6(d)]: No current flows in the diode bridge, and hence, the SRC in the MPC is essentially inactive in this mode. In other words, this operation mode is identical to the off-period of ordinary PWM converters—i_{Lmg} still linearly declines.

Overall, L_{kg} and C_r resonate in Modes 1 and 3, whereas L_{mg} does not contribute to the resonant operation. Hence, the resonant operation in the proposed MPC is similar to the SRC, not LLC converters that utilize L_{mg} for their resonant operation. Modes 1–2 and 3–4 are equivalent to the on- and off-period of ordinary PWM converters, while the SRC in the proposed MPC is active only in Modes 1 and 3. In the proposed MPC, the PWM and PFM controls are employed to regulate the battery voltage V_{bat} and output voltage V_{out} individually—d and f_S for V_{bat} and V_{out}, respectively. As long as Modes 2 and 4 exist, the operation

of the SRC is unaffected by that of the PWM converter because Modes 2 and 4 buffer duty cycle variation; one switching cycle contains one resonant period regardless of duty cycle variations as long as Modes 2 and 4 exist. In other words, the SRC can operate independently on d of the PWM converter, hence achieving decoupled regulation for V_{out} and V_{bat} as long as an operation criterion (see Section IV-B) is satisfied.

B. PWM Converter

The PWM converter in the proposed MPC operates similarly to the ordinary ones, except for the current superposition in Modes 1 and 3 [see Fig. 5(a)]. The voltage conversion ratio of the PWM converter is given by

$$V_{bat} = dV_{in}. \tag{8}$$

To achieve the decoupled output regulation, Modes 2 and 4 must exist, as mentioned in the previous subsection. In other words, half the resonant period must be shorter than both dT_S and $(1-d)T_S$. To this end, the following operation criterion must be satisfied;

$$1-\frac{f_S}{2f_r} > d > \frac{f_S}{2f_r}. \tag{9}$$

In the proposed MPC, d is manipulated in the range of (9) to regulate V_{bat}, according to (8). In the meantime, f_S is adjusted to regulate V_{out}, as will be explained in the next subsection. As long as this operation criterion (9) is satisfied, the PWM converter and SRC in the proposed MPC can operate independently, achieving the decoupled regulation for V_{out} and V_{bat}.

C. Series-Resonant Converter (SRC)

As mentioned in Section IV-A, no current flows in Modes 2 and 4 in the SRC. By neglecting these inactive periods, as shown in Fig. 7(a), currents and voltages in the SRC can be approximated to be sinusoidal and square voltage waves with

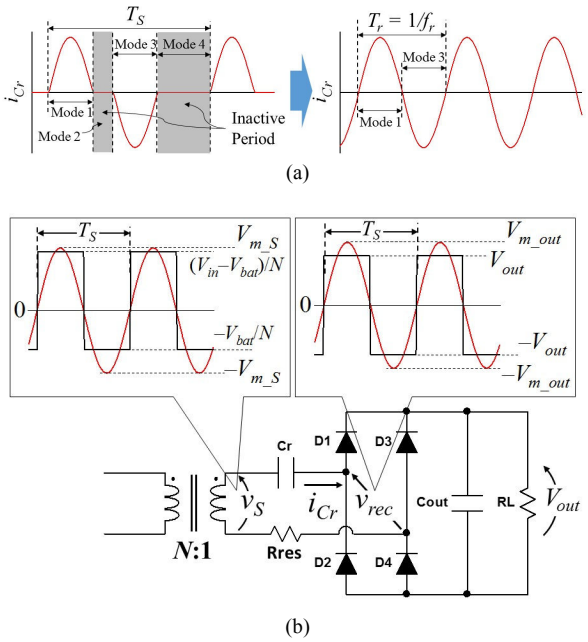

Fig. 7. (a) Current approximation and (b) equivalent circuit of SRC.

50% duty, simplifying the analysis. In this subsection, the operation analysis is performed focusing only on the secondary side, as shown in Fig. 7(b).

Based on the fundamental harmonics approximation (FHA), the square wave voltages produced across the secondary winding and rectifier bridge, v_S and v_{rec}, can be transformed into sinusoidal waves with voltage amplitudes of V_{m_S} and V_{m_out}, respectively [see Fig. 7(b)];

$$\begin{cases} v_S = V_{m\_S}\sin\omega_r t = \dfrac{2}{\pi}\dfrac{V_{in}}{N}\sin\omega_r t \\ v_{rec} = V_{m\_out}\sin\omega_r t = \dfrac{2}{\pi}2\left(V_{out}+2V_D\right)\sin\omega_r t \end{cases}. \tag{10}$$

where V_D is the forward voltage drop of diodes. The current amplitude of i_{Cr}, I_m [see Fig. 5(a)], can be yielded from (10) as

$$I_m = \frac{\dfrac{2}{\pi}\left(\dfrac{V_{in}}{N}-2\left(V_{out}+2V_D\right)\right)}{|Z|} = \frac{\dfrac{2}{\pi}\left(\dfrac{V_{in}}{N}-2\left(V_{out}+2V_D\right)\right)}{R_{res}}, \tag{11}$$

where Z is the characteristic impedance of the resonant tank, and R_{res} is the total resistance of the resonant current path containing the resonant tank. Meanwhile, the charge delivered through C_r during Modes 1 and 3, Q_{Cr}, is

$$Q_{Cr} = \int_0^{0.5/f_r} I_m \sin\omega_r t dt = \frac{I_m}{\pi f_r}. \tag{12}$$

The average output current I_{out} can be expressed using Q_{Cr} as

$$I_{out} = \frac{2Q_{Cr}}{T_S}. \tag{13}$$

From (12) and (13),

$$I_m = \frac{\pi f_r}{2f_S} I_{out}. \tag{14}$$

Substitution of (14) into (11) with the relationship of $V_{out} = I_{out}R_L$ yields

$$V_{out} = \frac{1}{N}\frac{4R_L V_{in} - 16R_L V_D}{\pi^2 R_{res}\dfrac{f_r}{f_S} + 8R_L}. \tag{15}$$

This equation does not contain d, suggesting the proposed MPC is capable of the decoupled regulation of V_{out} on V_{bat}. The equations derived here are valid at any d as long as (9) is satisfied.

D. Gain Characteristic of SRC

To discuss the gain characteristic of the SRC, the normalized switching frequency F is defined as

$$F = \frac{f_S}{f_r}. \tag{16}$$

From (15), the input-to-output voltage gain M is yielded as

$$M = \frac{V_{out}}{V_{in}} = \frac{1}{N}\frac{1-4\dfrac{V_D}{V_{in}}}{\dfrac{\pi^2 Q}{4F}+2}, \tag{17}$$

where Q is the quality factor defined as

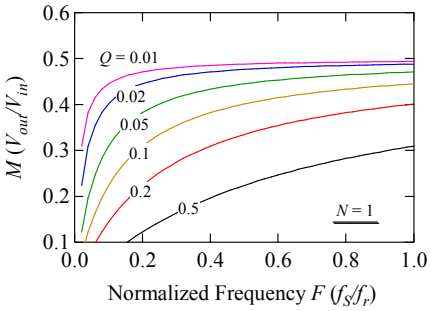

Fig. 8. Gain characteristics of SRC in the proposed MPC.

$$Q = \frac{R_{res}}{R_L}. \tag{18}$$

The theoretical gain characteristic of (17) with $N = 1$ is shown in Fig. 8. Similar to conventional SRCs, M is dependent on Q and decreases as F moves away from 1. Conventional SRCs usually operate with $F > 1$ to ensure soft-switching operations, whereas F for the SRC in the proposed MPC must be smaller than 1 because of the duty cycle limitation of (9). For the duty cycle variation range of 30–70%, for example, F must be smaller than 0.6, according to (9) and (16). This suggests that the allowable switching frequency range of the SRC in the MPC is influenced by the operation range of the PWM converter (i.e., duty cycle variations). Thus, the operation range of the SRC in the MPC is narrower than that of individual SRCs.

V. Battery Discharging Mode

A. Optimized Switching Frequency PWM Control

The battery V_{bat} is the input source for the MPC in the battery discharging mode, as shown in Fig. 4(c). The bidirectional PWM converter behaves as a synchronous boost converter, and therefore, it operates in CCM. There are two control freedoms of d and f_S in the proposed MPC, whereas the MPC in the battery discharging mode is essentially a single-input–single-output converter. In the battery discharging mode, two control freedoms can be used for V_{out} regulation.

As discussed in Section IV-C, Modes 2 and 4 in the battery charging mode are inactive for the SRC. These inactive periods should be as short as possible to reduce the RMS current of the SRC as well as associated Joule losses. To this end, f_S is adjusted so that dT_S or $(1 - d)T_S$ be equal to half the resonant period, expressed as

$$f_S = 2f_r\{0.5 - |d - 0.5|\}. \tag{19}$$

From the substitution of (16) into (19), the optimum F as a function of d is derived, as shown in Fig. 9. F peaks at $d = 50\%$ and decreases as d moves away from 50%. Although not mandatory, operating the MPC with (19) improves power conversion efficiencies in the battery discharging mode.

B. Operation Principle

The key operation waveforms in the battery discharging mode is shown in Fig. 5(b). The fundamental operation in the battery discharging mode is very similar to that in the battery

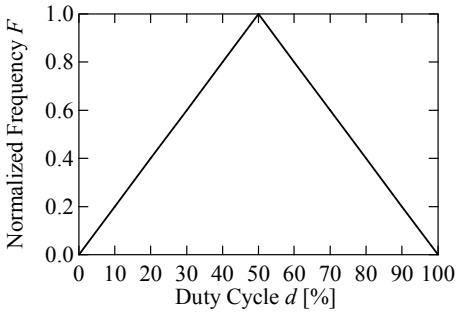

Fig. 9. Optimized F as a function of duty cycle d in battery discharging mode.

charging mode. The reverse blocking diode D_{block} prevents reverse power flow toward the input power source (e.g., solar panels). The major difference is that one of the inactive periods, which are found in the battery charging mode [Fig. 5(a)], is eliminated. In this subsection, the operation modes of the MPC is briefly explained assuming the case of $d < 0.5$.

Mode 1 [Fig. 10(a)]: Q_H is on, and i_{Lmg} linearly increases. $V_{in} - V_{bat}$ is applied to v_L, driving the SRC. L_{kg} and C_r resonate, and sinusoidal current of i_{Cr} flows through D_1 and D_4. i_{QH} is equal to i_{Lmg} with i_{Cr}/N superimposed on it. As the input port is opened in the battery discharging mode, the average of i_{QH} must be zero.

Mode 2 [Fig. 10(b)]: As i_{Cr} reaches zero, Q_H and Q_L are tuned-off and -on, respectively. i_{Lmg} starts linearly decreasing, and the polarity of v_L is reversed as $-V_{bat}$. i_{Cr} flows in the opposite direction as that in Mode 1 and through D_2 and D_3. As i_{Cr} becomes zero again, the operation shifts to the next mode.

Mode 3 [Fig. 10(c)]: i_{Lmg} still linearly decreases, while no

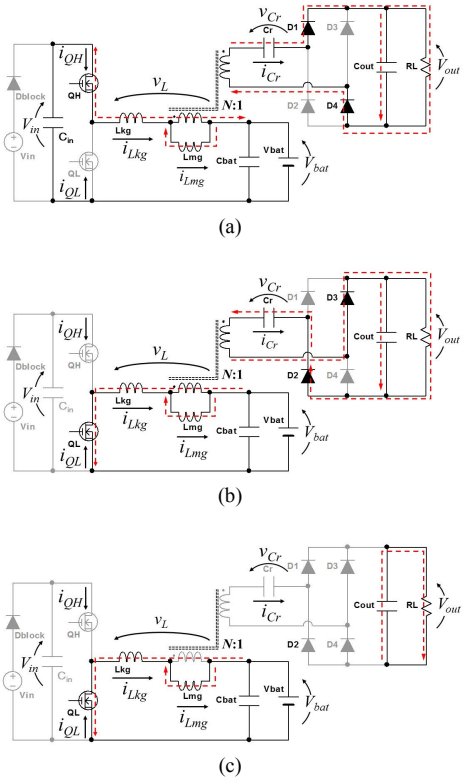

Fig. 10. Operation modes in battery discharging mode when $d < 0.5$: (a) Mode 1, (b) Mode 2, (c) Mode 3.

current flows on the secondary side. Hence, the SRC in the MPC is essentially inactive in this mode.

Overall, the MPC in the battery discharging mode operates as a boost-SRC, in which L_{mg} and C_{in} behave as a boost inductor and clump capacitor. Since P_{in} is zero, and C_{in} functions as a clump capacitor in the battery discharging mode, the average of the high-side switch current i_{QH} is zero, as can be seen from Fig. 5(b). d and f_S are adjusted according to (19), and the voltage of C_{in}, V_{in}, simply obeys (8). The power from V_{bat} goes through the boost converter and SRC before reaching V_{out}. In other words, the battery discharging mode is virtually two-stage power conversion, and hence, a power conversion efficiency in the battery discharging mode tends to be lower than that in the battery charging mode, even with the optimized switching frequency PWM control strategy proposed in the previous subsection.

C. PWM Converter and SRC

The equations derived for the battery charging mode are also valid for the battery discharging mode. The voltage of C_{in}, V_{in}, can be expressed using (8), and therefore, V_{out} in the battery discharging mode is given by the combination of (8) and (15).

VI. Design Guideline

A. Design Procedure

The design procedure for the proposed MPC is as follows;

1) Determine the duty cycle variation range from a given specification of V_{in} and V_{bat}

2) The turns ratio N and range of F are determined using (17) from a given specification of V_{in} and V_{out}, and check whether the operation criterion (9) is satisfied

3) Determine the resonant frequency f_r provisionally based on the target range of switching frequency f_S

4) L_{mg} is designed so as to fulfill a ripple current requirement

5) Make a transformer, and measure its L_{kg} and L_{mg}

6) Chose C_r, and determine practical f_r as well as f_S

In the following, a step-by-step design procedure is exemplified for a target specification of V_{in} = 36 V, V_{bat} = 12–16 V and I_{bat} = 5.0 A, and V_{out} = 42–45 V and R_L = 30–100 Ω at $f_S \leq$ 100 kHz.

Step 1): From the specification, the duty cycle variation range is 0.33–0.44.

Step 2): Iterative design is necessary for this step because the gain M is not only non-linear as shown in Fig. 8 but also dependent on R_{res} [see (17) and (18)], which is an unknown parameter until a transformer is practically made. From the target specification and gain characteristics (see Fig. 16 that shows not only experimental but also theoretical gain characteristics) from the measured R_{res} of the practical transformer, N and the range of F were determined to be 0.36 and 0.2–0.6, respectively. The determined range of F satisfies (9).

Step 3): An initial target was $f_S \leq$ 100 kHz. To achieve the operation at $0.2 < F < 0.6$, f_r was provisionally determined to be 167 kHz.

Step 4): In general, a ripple current factor of a filter inductor in ordinary PWM converters is around 30%. A required inductance value of L_{mg} is given by

$$L_{mg} = \frac{V_{in} - V_{bat}}{I_{ripple}} dT_S = \frac{V_{in} d(1-d)}{I_{ripple} F f_r}, \tag{20}$$

where I_{ripple} (= $0.3I_{bat}$) is the ripple current of L_{mg}. As this equation indicates, L_{mg} becomes large at low F, likely resulting in increased volume of the transformer. In this design procedure, we determined L_{mg} at the central value of F (i.e., F = 0.4), as L_{mg} = 75–83 μH.

Step 5): The transformer was made with the determined parameters of N = 0.36 and target L_{mg} of 75–83 μH. The actual values of L_{kg} and L_{mg} were measured to be 0.55 μH and 96.4 μH, respectively.

Step 6): According to the provisionally determined f_r of 167 kHz, C_r = 220 nF was selected. Therefore, the actual f_r was 176 kHz based on (5). From f_r = 176 kHz and F = 0.6, f_S was finally determined to be 105 kHz.

B. Transformer

As mentioned in Section II-A, the transformer in the proposed MPC plays two roles of a filter inductor for the PWM converter and resonant inductor for the SRC. Hence, the transformer should be properly designed so that both L_{mg} and L_{kg} are a desirable value. The transformer for the proposed MPC can be designed very similarly to that for LLC resonant converters [32], for which both L_{kg} and L_{mg} are utilized to obtain desired gain characteristics.

In addition to the sinusoidal current for the SRC, the dc current also flows through the transformer primary winding, and therefore, a gap is necessary to prevent saturation of the core by the peak current of i_{Lmg}. The volume of the transformer would be larger than that of the conventional one shown in Fig. 2 because of the relatively large peak of i_{Lmg} (or high flux density), but the conventional MPC requires two separate magnetic components. Quantitative comparison on total core volume between the proposed and conventional MPCs needs to be performed, which will be a part of our future works.

C. Switches

The voltage stress of switches is equal to V_{in}, similar to traditional PWM converters. The peak current of the low-side switch Q_L is identical to that in traditional PWM converters. The high-side switch Q_H, on the other hand, should be selected with considering the current superposition as can be seen in Fig. 5(a). i_{QH} (as well as i_{Lkg}) becomes maximum at $t = T_r/4$ (T_r being the resonant period) due to the superimposed resonant current of i_{Cr}/N. As shown in Fig. 5(a), i_{QH} is equal to i_{Lkg} in Modes 1–2, and from (4), (14), and (16), the peak value of i_{QH}, I_{QH_peak}, is yielded as

$$I_{QH\_peak} = i_{Lmg}(0.25T_r) + \frac{\pi}{2NF} I_{out}. \tag{21}$$

D. Diodes

The peak current of diodes is equal to I_m [see Fig. 5(a)] that is expressed as (14). The voltage stress of diodes is V_{out}, similar to

TABLE I
LOSS COMPONENTS IN THE PROPOSED MPC

Diode Conduction Loss		$2I_{out}V_D$
Switching Loss		$\frac{V_{in}I_{bat}(T_{rise}+T_{fall})f_S}{2}$ T_{rise}: Rise Time, T_{fall}: Fall Time
Joule Loss	Primary Winding	$\left(\frac{f_r}{f_S}\frac{\pi^2}{8N^2}I_{out}^2+I_{Bat}^2\right)r_{primary}$
	Secondary Winding	$\frac{f_r}{f_S}\frac{\pi^2 I_{out}^2}{8}r_{secondary}$
	High-Side Switch, Q_H	$\left\{\frac{f_r}{f_S}\frac{\pi^2 I_{out}^2}{16N^2}+\frac{I_{out}I_{Bat}}{N}+I_{Bat}^2 d\right\}r_{on}$
	Low-Side Switch, Q_L	$\left\{\frac{f_r}{f_S}\frac{\pi^2 I_{out}^2}{16N^2}-\frac{I_{out}I_{Bat}}{N}+I_{Bat}^2(1-d)\right\}r_{on}$
	Resonant Capacitor, C_r	$\frac{f_r}{f_S}\frac{\pi^2 I_{out}^2}{8}r_{Cr}$
	Output Capacitor, C_{out}	$\left(\frac{f_r}{8f_S}-\frac{4}{\pi}+1\right)I_{out}^2 r_{Cout}$
	Input Capacitor, C_{in}	$\left\{\frac{f_r}{f_S}\frac{\pi^2}{16N^2}I_{out}^2-\frac{I_{out}(I_{bat}-I_{in})}{N}+d\left(I_{bat}^2-2I_{bat}I_{in}\right)+I_{in}^2\right\}r_{Cin}$

ordinary full-bridge rectifiers.

E. Loss Model

The diode conduction loss is generally proportional to its average current. The switching loss can be modeled as [33]. Joule loss models can be derived from instantaneous currents expressed in Section IV. Obtaining each loss model is a tedious and lengthy process, and hence, detailed derivation procedures are omitted in this paper. Loss components in the proposed MPC are summarized in Table I.

VII. EXPERIMENTAL RESULTS

A. Prototype and Controller

A 150-W prototype (P_{out} = 75 W and P_{bat} = 75 W) of the proposed MPC was built as shown in Fig. 11, and its component values are listed in Table II. L_{mg} and L_{kg} of the transformer were measured using an LCR meter with open-circuit and short-circuit terminals of the secondary winding. The prototype was designed for V_{in} = 36 V, V_{bat} = 12–16 V, and V_{out} = 42–45 V, and its resonant frequency f_r was 176 kHz. According to the operation criterion of (9), the frequency range in the battery charging mode was determined to be $0.2 \le F \le 0.6$. The prototype was controlled by PE-Expert 4 employing TMS320C6657 (Myway Plus Corporation, Japan).

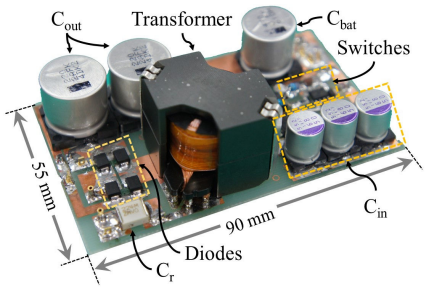

Fig. 11. Photograph of 150-W prototype.

TABLE II
COMPONENT VALUES

Component	Value
C_{in}	Aluminum Electrolytic Capacitor, 68 µF × 3, 40 mΩ
Q_H, Q_L	FDD390N15A, R_{on} = 33.4 mΩ
Transformer	$N_1:N_2$ = 9:25, L_{kg} = 0.55 µH, L_{mg} = 96.4 µH $r_{primary}$ = 35 mΩ, $r_{secondary}$ = 210 mΩ
C_{bat}	Almunum Electrolytic Capacitor, 470 µF
C_r	Film Capacitor, 220 nF, 45 mΩ
C_{out}	Almunum Electrolytic Capacitor, 220 µF × 2, 85 mΩ
D_1–D_4	Fast Recovery Diode, MURS110T3G, V_D = 0.88 V
Gate Driver	IRS2184S, Dead Time =400 ns

The control block diagram for the proposed MPC is shown in Fig. 12. In the battery charging mode, the battery current (I_{bat}) or voltage (V_{bat}) are regulated with PWM control while the output voltage (V_{out}) is control with PFM by adjusting f_S. In the battery discharging mode, both d and f_S are manipulated according to (19), as discussed in Section V-A.

B. Power Conversion Efficiency and Waveforms

Since the MPC has two output ports (i.e., V_{out} and V_{bat}), either P_{out} or P_{bat} was fixed while the rest was varied for the efficiency measurement. Power conversion efficiencies in the battery charging and discharging modes were measured. The key operation waveforms were also measured, as shown in Fig. 13. The measured waveforms agreed well with the theoretical ones shown in Figs. 5(a) and (b), verifying the operation of the

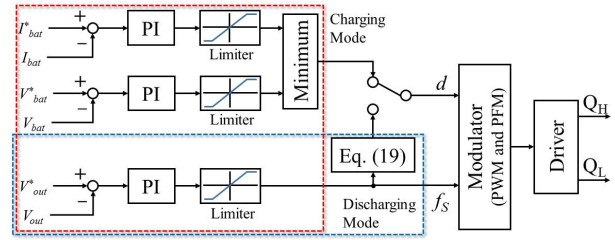

Fig. 12. Control block diagram.

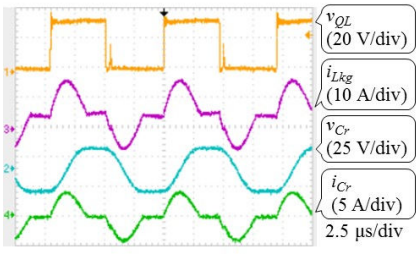

(a)

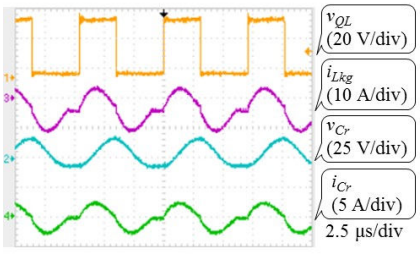

(b)

Fig. 13. Measured key waveforms in (a) battery charging mode at F = 0.6, d = 50%, P_{out} = 75 W, P_{bat} = 75 W, and (b) battery discharging mode at F = 0.8, d = 40%, P_{out} = 75 W.

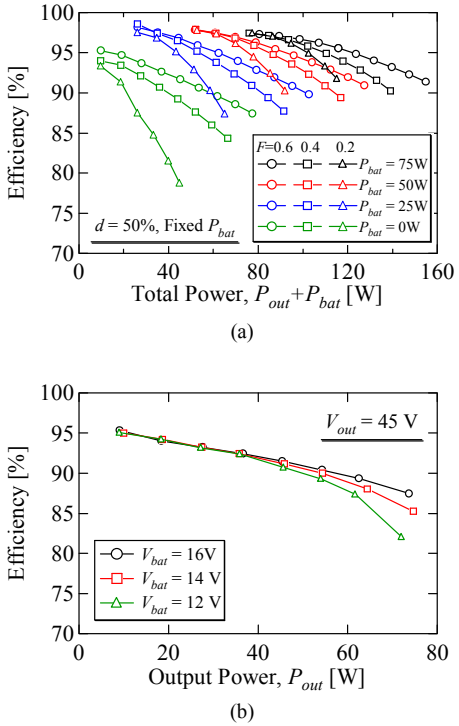

Fig. 14. Measured efficiencies as a function of total power in (a) battery charging mode at fixed P_{bat} and d = 50%, and (b) battery discharging mode.

prototype.

The measured efficiencies as a function of the total output power (P_{out} + P_{bat}) in the battery charging mode at fixed P_{bat} and d = 0.5 are shown in Fig. 14(a). The efficiencies declined as F decreased. The deteriorated efficiencies at low F were due to the increased peak current of the SRC, as (21) indicates—peak currents soar as F declines, increasing Joule losses. Another tendency found in Fig. 14(a) is that the efficiencies declined as the total power increased. Since P_{bat} was fixed, this tendency suggested the efficiency performance of the SRC was inferior to that of the PWM converter—the efficiencies of the PWM converter alone were approximately 97% while those of the SRC alone were merely 87.4% at P_{out} = 75 W.

Fig. 14(b) shows the measured efficiencies as a function of the output power in the battery discharging mode with V_{out} = 45 V. In comparison with the battery charging mode [e.g., P_{bat} = 75 W at F = 0.6 in Fig. 14(a)], the overall efficiencies in the battery discharging mode were inferior chiefly because the battery discharging mode is virtually the two-stage power conversion of the boost converter and SRC stages, as discussed in Section V-B.

The estimated loss breakdowns of the prototype in the battery charging mode are shown in Fig. 15. In addition to the diode conduction loss, which usually is the most dominant loss factor in ordinary converters, the Joule losses of the high-side switch Q_H and transformer's primary winding represented the significant portions of the total loss. This is due to the superposition of the sinusoidal resonant current of i_{Cr}/N on the triangular current wave of i_{Lmg}, as shown in Fig. 5(a).

The total loss increased with P_{out} [see Fig. 15(a)], whereas it remained nearly constant when P_{out} was fixed [see Fig. 15(b)].

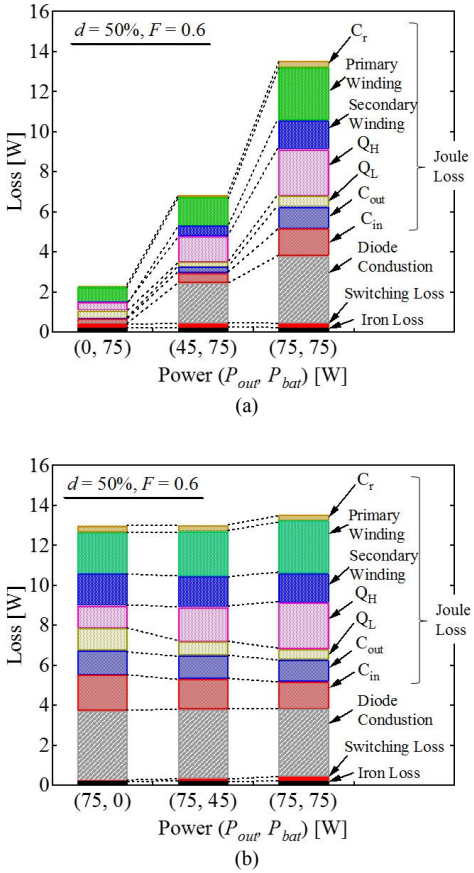

Fig. 15. Estimated loss breakdown in battery charging mode; (a) at varied Pout and fixed P_{bat} = 75 W, (b) at fixed P_{out} = 75 W and varied P_{bat}.

This tendency indicates the SRC represented the significant portion of the total loss. The increased Joule losses at the large-P_{out} region were due to the large RMS currents originating from the resonant operation of the SRC, as can be seen from Figs. 5(a) and 13(a).

C. Gain Characteristics of SRC

Gain characteristics of the SRC in the battery charging mode were measured at P_{bat} = 50 W and d = 50%. The results of the experiments and simulation using PSIM® are compared to the theoretical characteristics of (15), as shown in Fig. 16—(15) is the root equation for the gain characteristics shown in Fig. 8. The gain characteristics of the SRC were independent on d, as those at d = 30% and 50% were nearly identical. All the results matched very well, verifying the derived expressions in Section IV-C.

D. Interdependence between PWM Converter and SRC

To investigate the interdependence between two ports of V_{bat} and V_{out} in the battery charging mode, characteristics of V_{bat} and V_{out} were measured with varying F or d. The measured output characteristics as a function of d at fixed F and I_{bat} = 2.5 A are shown in Fig. 17. The measured V_{bat} showed the linear relationship with d at any F. Meanwhile, V_{out} was constant and independent on d.

The measured output characteristics as a function of F at d = 50% and P_{bat} = 50 W are shown in Fig. 18. Similar to the

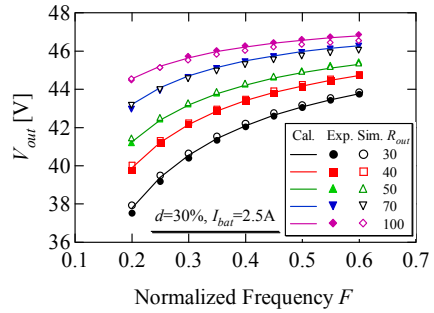

(a)

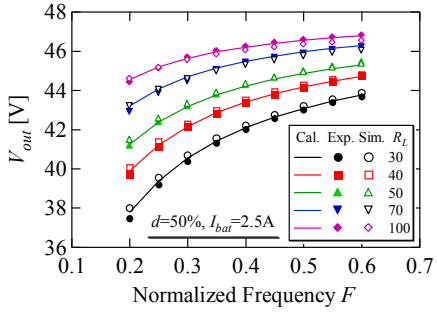

(b)

Fig. 16. Experimental, simulation, and theoretical gain characteristics of the SRC in the proposed MPC at (a) d = 30% and (b) d = 50%.

characteristics shown in Figs. 8 and 16, V_{out} was F-dependent. On the other hand, V_{bat} slightly declined as F increased probably because of the increased switching and Joule losses at higher F—higher losses result in decreased output voltage at the same power. Although slightly influenced, the characteristics of V_{bat} were nearly independent on F. The results shown in Figs. 17 and 18 demonstrated that V_{bat} and V_{out} can be individually regulated by PWM and PFM controls, respectively, achieving the decoupled output regulation.

E. Response to Load Transient

To demonstrate the decoupled output regulation in the battery charging mode, transient response characteristics of the MPC were measured with applying step changes in I_{out} and I_{bat}. An electronic load operating in resistance mode was used to emulate the step changes. V_{out} was regulated to be 45 V, while V_{bat} was controlled to be 16 V during the step change in I_{bat}, although both V_{bat} and I_{bat} need to be controlled in practical use as shown in Fig. 12.

The measured transient characteristics are shown in Fig. 19. At the moment of the step increase in I_{out}, as shown in Fig. 19(a), V_{out} dropped and F immediately increased (not shown) in response to the abrupt increase in I_{out}, while V_{bat} was unaffected, demonstrating that PWM-controlled V_{bat} was independent on PFM-controlled V_{out}. Similarly, the influence of the step increase in I_{bat} on V_{out} was trivial, as shown in Fig. 19(b). These results indicate that PFM-controlled V_{out} and PWM-controlled V_{bat} are nearly independent during transients, demonstrating the decoupled output regulation of the proposed MPC.

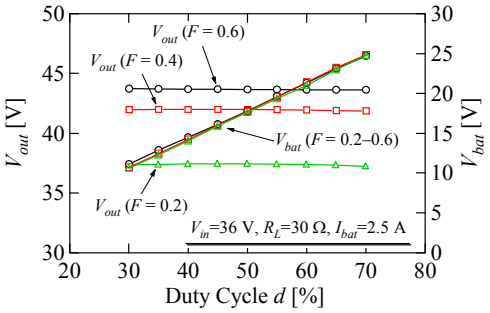

Fig. 17. Measured characteristics of V_{out} and V_{bat} with fixed F and varying d.

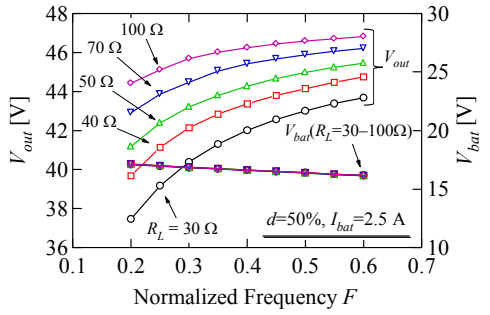

Fig. 18. Measured characteristics of V_{out} and V_{bat} with fixed d and varying F.

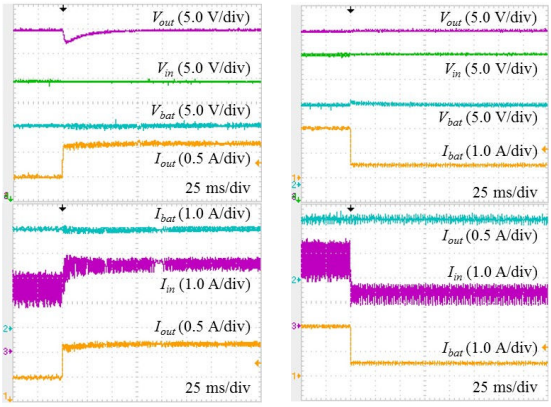

(a) (b)

Fig. 19. Measured transient response characteristics: (a) step-change in I_{out}, (b) step-change in I_{bat}.

VIII. Comparison

The proposed MPC is compared with conventional partially-isolated MPCs in terms of component count, modulation employed, and decoupled regulation capability in Table III. The PWM-controlled MPCs [17], [18] are relatively simple circuits, but their feedback loop design would be a challenging task to achieve decoupled regulation; a decoupling network needs to be derived from a complex state-space modeling to realize decoupled regulation [17]. MPCs utilizing both PWM and phase-shift (PS) controls [23]–[29] are capable of decoupled regulation depending on operation conditions, whereas their circuit complexity tends to increase as they require at least four switches for PS control—in general, PS-controlled converters require two legs, each consisting of

TABLE III
COMPARISON BETWEEN PROPOSED AND CONVENTIONAL PARTIALLY-ISOLATED MPCS

Topology	Component Count					Modulation Scheme	Decoupled Regulation	Reported Efficiency
	Switch	Diode	Capacitor	Inductor	Transformer			
[17]	3	2 (SR)	3	1	1 (CT)	PWM	No	
[18]	2	2	5	1	1	PWM	No	73–94%
[23]	4	2	3	0	1 (CT)	PWM and PS	Yes	75–90%
[26]	4	4	3	0	2	PWM and PS	Yes	87–91%
[27]	6	2	3	3	1	PWM and PS	Yes	93–97%
[28]	4	2	4	0	2	PWM and PS	Yes	86–91%
[29]	4	4	3	2	1	PWM and PS	Yes	91–97.5%
[30]	4	4	4	2	1	PWM and PFM	No	90–96%
Proposed	2	4	4	0	1	PWM and PFM	Yes	73–97%

SR: Synchronous Rectifier, CT: Center-Tapped, PS: phase-shift

two switches.

Meanwhile, the proposed MPC achieves decoupled regulation with only two switches as PFM control can be implemented with only one single leg. In addition to the simple topology, the miniaturized design is also feasible as the magnetic component count is only one because the transformer plays two roles, and its L_{kg} and L_{mg} are utilized for PFM and PWM controls, respectively. The proposed MPC is considered best suitable for relatively low-power applications, such as stand-alone photovoltaic systems, where the circuit simplicity and compactness are of great importance. Meanwhile, topologies based on interleaved PWM converters using more than four switches, such as [23]–[30], are naturally suitable for large-power applications as their current capability is simply doubled compared to ordinary PWM converters.

IX. CONCLUSIONS

The partially-isolated single-magnetic MPC integrating an SRC and PWM converter has been proposed. The transformer's magnetizing inductance is utilized as a filter inductor for the PWM converter, while the leakage inductance forms a resonant tank for the SRC, achieving the single-magnetic topology.

The detailed operation analysis was performed, and the mathematical model of the MPC was derived. The output and battery voltages are regulated with PFM and PWM controls, respectively, in the battery charging mode, in which the input power source supplies both the output and battery charging powers. In the battery discharging mode, on the other hand, the battery alone supplies the output power, and the output voltage is regulated by the optimized switching frequency PWM control scheme.

The experimental verification tests were performed using the 150-W prototype of the proposed MPC. The measured voltage conversion and transient response characteristics demonstrated that the output and battery voltages could be independently controlled by PFM and PWM controls, respectively, without interdependence.

APPENDIX

Although the waveforms of the proposed MPC may look similar to those of a conventional LLC converter, the operation principle is totally different. The major difference is that the magnetizing inductance L_{mg} does not contribute to the resonant operation of the proposed MPC.

Certain operation modes of the traditional LLC converter and proposed MPC are compared in Fig. 20; diode rectifiers on the secondary side are off in both converters. In the traditional LLC converter [see Fig. 20(a)], the current of L_{mg}, i_{Lmg}, flows through the resonant capacitor C_r, meaning L_{mg} resonates with C_r. Meanwhile, in the proposed MPC as shown in Fig. 20(b), no current flows through C_r, indicating L_{mg} does not resonate with C_r. Since L_{mg} does not resonate with C_r, the proposed MPC can be considered as an SRC.

REFERENCES

[1] J.L. Duarte, M. Hendrix, and M.G. Simoes, "Three-port bidirectional converter for hybrid fuel cell systems," *IEEE Power Electron.*, vol. 22, no. 2, pp. 480–487, Mar. 2007.

[2] C. Zhao, S. D. Round, and J. W. Kolar, "An isolated three-port bidirectional dc–dc converter with decoupled power flow management," *IEEE Ind. Electron.*, vol. 23, no. 5, pp. 2443–2453, Sep. 2008.

[3] H. Tao, J.L. Duarte, and M.A.M. Hendrix, "Three-port triple-half-bridge bidirectional converter with zero-voltage switching," *IEEE Power Electron.*, vol. 23, no. 2, pp. 782–792, Mar. 2008.

[4] H. Tao, A. Kotsopoulos, J.L. Duarte, and M.A.M. Hendrix, "Transformer-coupled multiport ZVS bidirectional dc–dc converter with wide input range," *IEEE Power Electron.*, vol. 23, no. 2, pp. 771–781, Mar. 2008.

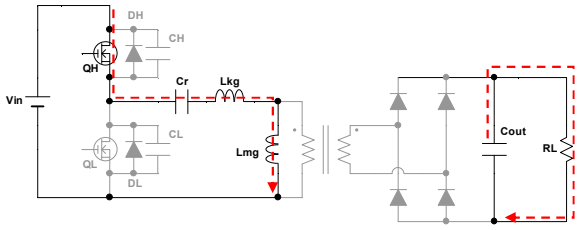

(a)

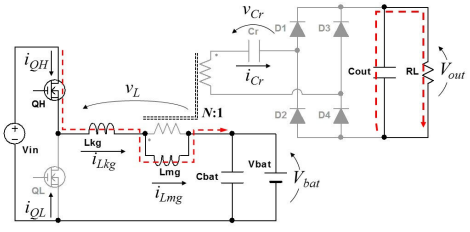

(b)

Fig. 20. Comparison on resonant operations between LLC converter and proposed MPC; (a) Certain operation mode in LLC converter, (b) Mode 2 [Fig. 6(b)].

[5] H. Krishnaswami and N. Mohan, "Three-port series-resonant dc–dc converter to interface renewable energy sources with bidirectional load and energy storage ports," *IEEE Power Electron*., vol. 24, no. 10, pp. 2289–2297, Oct. 2009.
[6] M. Marchesoni and C. Vacca, "New dc–dc converter for energy storage system interfacing in fuel cell hybrid electric vehicles," *IEEE Trans. Power Electron*., vol. 22, no. 1, pp. 301–308, Jan. 2007.
[7] K. Gummi and M. Ferdowsi, "Double-input dc–dc power electronic converters for electric-drive vehicles—topology exploration and synthesis using a single-pole triple-throw switch," *IEEE Trans. Ind. Electron*., vol. 57, no. 2, pp. 617–623, Feb. 2010.
[8] C.N. Onwuchekwa and A. Kwasinski, "A modified-time-sharing switching technique for multiple-input dc-dc converters," *IEEE Trans. Power Electron*., vol. 27, no. 11, pp. 4492–4502, Nov. 2012.
[9] A. Nahavandi, M. T. Hagh, M. B. B. Sharifian, and S. Danyali, "A nonisolated multiinput multioutput dc–dc boost converter for electric vehicle applications," *IEEE Trans. Power Electron*., vol. 30, no. 4, pp. 1818–1835, Apr. 2015.
[10] P. Yang. C. K. Tse, J. Xu, and G. Zhou, "Synthesis and analysis of double-input single-output dc/dc converters," *IEEE Trans. Ind. Electron*., vol.62, no. 10, pp. 6284–6295, Oct. 2015.
[11] A. Hintz, U. R. Prasanna, and K. Rajashekara, "Novel modular multiple-input bidirectional dc–dc power converter (MIPC) for HEV/FCV application," *IEEE Ind. Electron*., vol. 62, no. 5, pp. 3068–3076, May 2015.
[12] H. Zhu, D. Zhang, B. hang, and Z. Zhou, "A nonisolated three-port dc–dc converter and three-domain control method for PV-battery power systems," *IEEE Trans. Ind. Electron*., vol. 62, no. 8, pp. 4937–4947, Aug. 2015.
[13] H. Zhu, D. Zhang, Q. Liu, and Z. Zhou, "Three-port dc/dc converter with all ports current ripple cancellation using integrated magnetic technique," *IEEE Trans. Ind. Electron*., vol. 31, no. 3, pp. 2174–2186, Mar. 2016.
[14] R.R. Ahrabi, H. Ardi, M. Elmi, and A. Ajami, "A novel step-up multiinput dc–dc converter for hybrid electric vehicles application," *IEEE Trans. Power Electron*., vol. 32, no. 5, pp. 3549–3561, May 2017.
[15] N. D. Benavides and P. L. Chapman, "Power budgeting of a multiple-input buck-boost converter," *IEEE Trans. Ind. Electron*., vol. 20, no. 6, pp. 1303–1309, Nov. 2005.
[16] S.Y. Yu and A. Kwasinski, "Analysis of soft-switching isolated time-sharing multiple-input converters for dc distribution systems," *IEEE Trans. Power Electron*., vol. 28, no. 4, pp. 1783–1794, Apr. 2013.
[17] Z. Qian, O.A. Rahman, H.A. Atrach, and I. Batarseh, "Modeling and control of three-port dc/dc converter interface for satellite applications," *IEEE Trans. Power Electron*., vol. 25, no. 3, pp. 637–649, Mar. 2010.
[18] D. Debnath and K. Chatterjee, "Two-stage solar photovoltaic-based stand-alone scheme having battery as energy storage element for rural deployment," *IEEE Trans. Ind. Electron*., vol. 62, no. 7, pp. 4148–4157, Jul. 2015.
[19] H. Wu, R. Chen, J. Zhang, Y. Xing, H. Hu, and H. Ge, "A family of three port half-bridge converters for a stand-alone renewable power system," *IEEE Trans. Power Electron*., vol. 26, no. 9, pp. 2697–2706, Sep. 2011.
[20] J.K. Kim, J.B. Lee, and G.W. Moon, "Zero-voltage switching multioutput flyback converter with integrated auxiliary buck converter," *IEEE Trans. Power Electron*., vol. 29, no. 6, pp. 3001–2943, Jun. 2014.
[21] Q. Wang, J. Zhang, X. Ruan, and K. Jin, "Isolated single primary winding multiple-input converters," *IEEE Trans. Power Electron*., vol. 26, no. 12, pp. 3435–3442, Dec. 2011.
[22] G. J. Su, and L. Tang, "A multiphase, modular, bidirectional, triple-voltage dc–dc converter for hybrid and fuel cell vehicle power systems," *IEEE Trans. Power Electron*., vol. 23, no. 6, pp. 3035–3046, Nov. 2008.
[23] W. Li, J. Xiao, Y. Zhao, and X. He, "PWM plus phase angle shift (PPAS) control scheme for combined multiport dc/dc converters," *IEEE Trans. Power Electron*., vol. 27, no. 3, pp. 1479–1489, Mar. 2012.
[24] H. Wu, K. Sun, R. Chen, H. Hu, and Y. Xing, "Full-bridge three-port converters with wide input voltage range for renewable power systems," *IEEE Trans. Power Electron*., vol. 27, no. 9, pp. 3965–3974, Sep. 2012.
[25] H. Wu, P. Xu, H. Hu, Z. Zhou, and Y. Xian, "Multiport converters based on integration of full-bridge and bidirectional dc–dc topologies for renewable generation systems," *IEEE Trans. Ind. Electron*., vol. 61, no. 2, pp. 856–869, Feb. 2014.
[26] W. Li, C. Xu, H. Luo, Y. Hu, X He, and C. Xia, "Decoupling-controlled triport composited dc/dc converter for multiple energy interface," *IEEE Trans. Ind. Electron*., vol. 62, no. 7, pp. 4504–4513, Jul. 2015.
[27] J. Zhang, H. Wu, X. Qin, and Y. Xing, "PWM plus secondary-side phase-shift controlled soft-switching full-bridge three-port converter for renewable power systems," *IEEE Trans. Ind. Electron*., vol. 62, no. 11, pp. 7072, Nov. 2015.
[28] Y. Hu, W. Xiao, W. Cao, B. Ji, D. J. Morrow, "Three-port dc–dc converter for stand-alone photovoltaic systems," *IEEE Trans. Power Electron*., vol. 30, no. 6, pp. 3068–3076, Jun. 2015.
[29] M. C. Mira, Z. Zhang, A. Knott, and M. A. E. Andersen, "Analysis, design, modeling, and control of an interleaved-boost full-bridge three-port converter for hybrid renewable energy systems," *IEEE Trans. Power Electron*., vol. 32, no. 2, pp. 1138–1155, Feb. 2017.
[30] X. Sun, Y. Shen, W. Li, and H. Wu, "A PWM and PFM Hybrid Modulated Three-Port Converter for a Standalone PV/Battery Power System," *IEEE J. Emerging Selected Topics Power Electron*., vol. 3, no. 4, pp. 984–1000, Dec. 2015.
[31] V.L. Tran, H.N. Vu, D.D. Tran, and W. Choi, "Design and implementation of a high-efficiency multiple output charger based on the time-division multiple control technique," *IEEE Trans. Power Electron*., vol. 32, no. 2, pp. 1210–1219, Feb. 2017.
[32] TDK. (2010, Sep.) LLC Resonant Power Transformers. [Online]. available: http://www.ic-contract.ru/images/pdf/TDK/e636_srx.pdf#search='TDK+LLC+transforme
[33] Rohm (2016, Oct.) Calculation of Power Loss (Synchronous). [Online]. available: http://rohmfs.rohm.com/en/products/databook/applinote/ic/power/switching_regulator/power_loss_appli-e.pdf#search=%27switching+loss%27

Masatoshi Uno (M'06) was born in Japan in 1979. He received the B.E. degree in electronics engineering and the M.E. degree in electrical engineering from Doshisha University, Kyoto, Japan, and the Ph.D. degree in space and astronautical science from the Graduate University for Advanced Studies, Hayama, Japan, in 2002, 2004, and 2012, respectively.

In 2004, he joined the Japan Aerospace Exploration Agency, Sagamihara, Japan, where he developed spacecraft power systems including battery, photovoltaic, and fuel cell systems. In 2014, he joined the Department of Electrical and Electronics Engineering, Ibaraki University, Ibaraki, Japan, where he is currently an Associate Professor of Electrical Engineering.

His research interests include switching power converters for renewable energy systems, life evaluation for supercapacitors and lithium-ion batteries, and development of spacecraft power systems. Dr. Uno is a member of the Institute of Electrical Engineers of Japan (IEEJ) and the Institute of Electronics, Information, and Communication Engineers (IEICE).

Rina Oyama was born in Japan in 1994. She received the B.E. degree in electrical engineering from Ibaraki University, Ibaraki, Japan, in 2017.

Since 2017, she has been an electrical engineer with Hitachi City Hall, Hitachi, Japan.

Kazuki Sugiyama was born in Japan in 1994. He received the B.E. degree in electrical engineering from Ibaraki University, Ibaraki, Japan, in 2016, where he is currently working toward the M.E. degree in the Graduate School of Science and Engineering.

His research interests include PWM- and PFM-switched capacitor converters for photovoltaic systems.